

Contact fracture of brittle bilayer coatings on soft substrates

Pedro Miranda

Departamento Electrónica e Ingeniería Electromecánica, Escuela de Ingenierías Industriales, Universidad de Extremadura, 06071 Badajoz, Spain

Antonia Pajares

Departamento de Física, Facultad de Ciencias, Universidad de Extremadura, 06071 Badajoz, Spain

Fernando Guiberteau

Departamento Electrónica e Ingeniería Electromecánica, Escuela de Ingenierías Industriales, Universidad de Extremadura, 06071 Badajoz, Spain

Francisco L. Cumbreira

Departamento de Física, Facultad de Ciencias, Universidad de Extremadura, 06071 Badajoz, Spain

Brian R. Lawn

Materials Science and Engineering Laboratory, National Institute of Standards and Technology, Gaithersburg, Maryland 20899

(Received 22 May 2000; accepted 21 September 2000).

Contact-induced fracture modes in trilayers consisting of a brittle bilayer coating on a soft substrate were investigated. Experiments were performed on model transparent glass/sapphire/polycarbonate structures bonded with epoxy adhesive, to enable *in situ* observation during the contact. Individual layer surfaces were preferentially abraded to introduce uniform flaw states and so allowed each crack type to be studied separately and controllably. Fracture occurred by cone cracking at the glass top surface or by radial cracking at the glass or sapphire bottom surfaces. Critical loads for each crack type were measured, for fixed glass thickness and several specified sapphire thicknesses. Finite element modeling (FEM) was used to evaluate the critical load data for radial cracking, using as essential input material parameters evaluated from characterization tests on constituent materials and supplemental glass/polymer and sapphire/polymer bilayer structures. The FEM calculations demonstrated pronounced stress transfer from the applied contact to the underlying sapphire layer, explaining a tendency for preferred fracture of this relatively stiff component. Factors affecting the design of optimal trilayer structures for maximum fracture resistance of practical layer systems were considered.

I. INTRODUCTION

Hard ceramic coatings on soft substrates are of technological importance for the protection they afford substrates against contacts, impacts, and thermal or chemical cycling. Practical examples of layer systems with ceramic coatings include cutting tools,¹ thermal barrier coatings,^{2,3} and dental crowns.^{4,5} An ideally hard coating protects the soft underlayer by maintaining the entire system in the elastic region. But hard coatings tend to be brittle and are subject to failure from transverse fracture or other damage modes, especially in contact loading where stress intensities are highly concentrated.⁶⁻¹⁶ The fracture modes include traditional cone or ring cracks that initiate from the top surface outside the contact area and deleterious radial cracks that initiate at the lower surface of the coating and spread radially outward on

median planes containing the load axis. Recent studies of model transparent glass/polymer bilayers have proved especially useful in evaluating such cracking modes *in situ* during contact loading and for quantifying the crack initiation conditions in terms of coating thickness and coating/substrate elastic mismatch.^{17,18}

In some cases a single brittle layer may not be adequate to preclude coating failure or to protect a soft substrate. It may be necessary to include a relatively stiff and strong intermediate layer for reinforcement and support, resulting in a trilayer structure. A weaker outer-layer may be retained for crack suppression,¹⁹ wear resistance, or aesthetics. Such bilayer coating systems are used in porcelain-based dental crowns, for instance, traditionally with the porcelain fused to a metal intermediate layer but more recently to a strong ceramic such as alumina.^{4,5} Yet the lifetimes of crown systems, especially those with ceramic intermediate layers, are

limited.²⁰ A systematic analysis of damage modes in all-ceramic brittle coating systems of this kind would appear to be desirable.

In the present work we study the mechanical response of a model glass/sapphire/polymer trilayer system subject to contact stresses generated in Hertzian indentation tests. The specific material constituents are again chosen for their transparency, enabling *in situ* observations of crack initiation and propagation during mechanical testing. The constituent coating materials (glass, sapphire) also have similar mechanical properties to those used in all-ceramic dental crowns (porcelain, alumina). A simple epoxy adhesive is used to bond the adjacent layers.¹⁸ Our study describes the morphology and location of competing transverse crack modes, with special attention to the more insidious radial cracking and to the corresponding critical initiation loads. We show that radial cracks may occur preferentially in the stiffer, intermediate sapphire layer rather than in the outer glass layer, even though the sapphire is several times stronger than the glass.

Finite element modelling (FEM) is used to compute critical loads for radial cracking in the trilayer structures for comparison with experimental values, using material parameters evaluated from characterization tests on constituent materials and supplemental glass/polymer and sapphire/polymer bilayer structures as essential data input. FEM is also used to demonstrate how the stresses from the applied contact transfer to the stiffer intermediate sapphire layer, explaining preferential fracture of this component. Implications for the design of optimal trilayer structures for maximum fracture resistance of practical layer systems are considered.

II. EXPERIMENTAL METHOD

A. Materials

Figure 1 shows a schematic of the model trilayer system fabricated for this study. Individual layers were obtained as smooth, flat plates, minimum surface dimensions 25×50 mm, as follows: *upper coating layers*, soda-lime glass microslides (Daigger and Co., Wheeling, IL), fixed thickness $d_g = 1000$ μm ; *intermediate coating layers*, synthetic sapphire plates, randomly oriented (Goodfellow Ltd., Cambridge, England), thicknesses $d_s = 350, 500, 800,$ and 920 μm ; *substrate layers*, polycarbonate polymer slabs (AIN Plastics, Norfolk, VA), fixed thickness 12.5 mm. Elastic moduli of these materials shown in Table I indicate the relative stiffnesses of the individual components. All materials were transparent.

A thin layer of epoxy adhesive (Harcos Chemicals, Bellesville, NJ) was placed between adjacent material layers and kept under light uniaxial pressure for 24 h, to produce trilayers consisting of glass/sapphire bilayer coatings on polycarbonate substrates. The thicknesses of

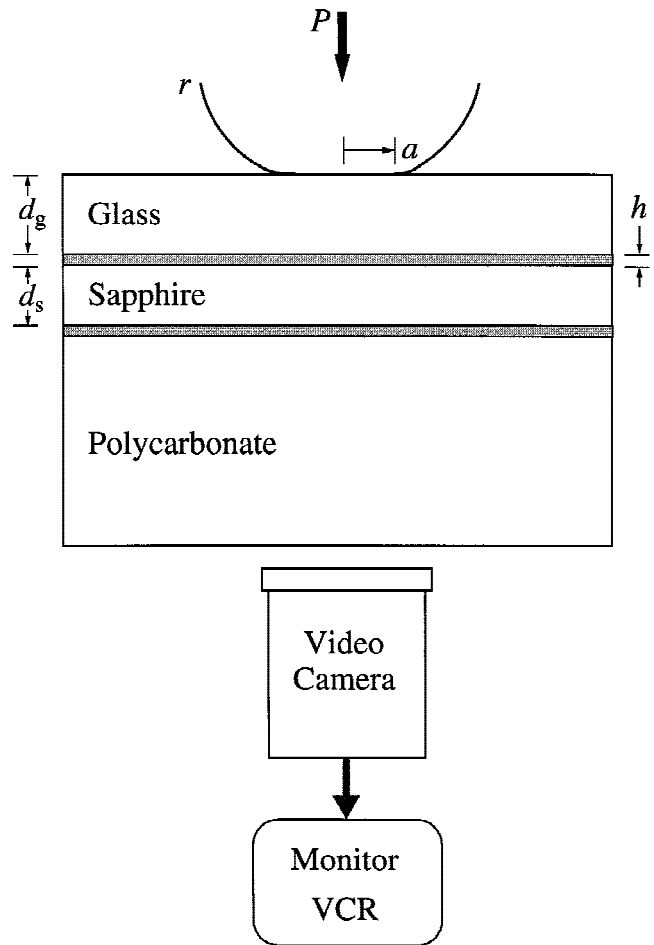


FIG. 1. Schematic of Hertzian contact test for glass/sapphire coating, thickness d_g/d_s , on polycarbonate substrate bonded with epoxy adhesive, thickness h . A tungsten carbide (WC) sphere of radius r produces contact of radius a at load P . A camera is used to monitor crack evolution optically *in situ* from below contact.

the adhesive interlayers, measured optically to within ± 2 μm after sectioning finished trilayers specimens, varied between 5 and 22 μm .

Prior to bonding, a designated surface of one of the two brittle layers was abraded with a slurry of 600 grit SiC, to enable independent observation of each fracture mode in the ensuing contact tests and to reduce scatter in the critical loads.¹⁷ Glass top surfaces, glass bottom surfaces, and sapphire bottom surfaces were abraded in this way. For comparison, some trilayers were bonded with all surfaces in their as-received states (i.e., no abrasion).

Some as-received monolithic glass, sapphire and polycarbonate specimens were set aside for characterization of individual materials constituents. Bulk specimens of the epoxy adhesive were prepared by pouring the viscous mixture into a mould and placing in an evacuation chamber for 10 min to remove excess bubbles, followed by curing for 2 days in laboratory atmosphere. Tungsten carbide specimens were cut from the largest indenters to be used in the contact tests.

TABLE I. Mechanical properties for constituent layer and indenter materials.^a

Material	Young's modulus E (GPa)	Poisson's ratio ν	Yield stress Y (GPa)	Strain-hardening coefficient α	Strength σ_F (GPa)
Soda-lime glass	73	0.22	135 ± 9
Sapphire	417	0.20	550 ± 63
Polycarbonate	2.23	0.35	0.065	0.050	...
Epoxy adhesive	3.7	0.35	0.093	0.001	...
Tungsten carbide	626	0.22	3.4	0.50	...

^aError bars in σ_F are uncertainties from evaluations in Fig. 10. Uncertainties in E and ν estimated at <5%, and in Y and α < 10%.

Single-layer glass and sapphire coating specimens on polycarbonate substrates were also prepared for subsidiary materials characterization, using the same adhesive bonding as above. Thicknesses were $d_g = 500$ and $1000 \mu\text{m}$ and $d_s = 350, 500, 800, 920,$ and $1460 \mu\text{m}$. Only the bottom surfaces of the layers were abraded in these specimens.

B. Hertzian contact: Crack morphology and critical loads

Hertzian contact tests were used to determine fracture behavior of the brittle coatings in the trilayers (Fig. 1). A tungsten carbide sphere of radius $r = 3.18 \text{ mm}$ was loaded onto the specimen top surface at peak loads P using a mechanical testing machine with load–time data acquisition software (Instron 5565, Instron Corp, Canton, MA), at crosshead speed 0.05 mm min^{-1} . A self-illuminating low-power zoom optical system (Zoom 70, OPTEM International, Fairport, NY) was used to observe the evolving cone and radial crack patterns from below the contact. The image was recorded via an analog camera (CV-730, JAI Corp., Yokohama, Japan) connected to a video recorder and TV monitor. The top contact surface of the glass layer was precoated with a thin (approximately 50 nm) gold film to enhance image intensity.

Selected indented specimens were *a posteriori* sectioned through the contact sites using a diamond saw and polished to $1\text{-}\mu\text{m}$ diamond paste to enable side views of the crack patterns.²¹ Where cone cracks formed, the section was taken down to the actual contact center and then given a light etch in 12% HF acid solution for 1 min. Where radial cracks formed, the section was made parallel to the median plane of one of these cracks, down to about 1 mm from the contact center.

Critical loads for first fracture in each trilayer, P_{cone} for cone cracks and P_{rad} for radial cracks, were measured from synchronized image sequences and Instron load–time records.

C. Hertzian contact: Subsidiary tests and material characterization

Indentation stress–strain curves^{22–25} were determined for each bulk monolithic material from measurements of contact load P and contact radius a for sphere radii r in

the range 1.98 to 12.7 mm , as indentation stress $p_0 = P/\pi a^2$ versus indentation strain a/r , using the same crosshead speed as above. These curves are needed for determining elastic–plastic input parameters for stress analysis (Sec. IV) and thence for determining whether any of the components in the trilayer structures exceed elastic limits in the tests. Precoating the specimen surfaces with gold in the glass, sapphire, and tungsten carbide specimens, and with ink in the polycarbonate and adhesive specimens, enhanced the contact areas in the elastic region.

Supplemental critical load P_{cone} measurements were made on glass and sapphire monolith specimens, to establish reference baselines for the trilayers. Analogous P_{rad} measurements were made on glass/polycarbonate and sapphire/polycarbonate bilayer specimens, for subsequent strength evaluations (Sec. IV).

III. EXPERIMENTAL RESULTS

A. Crack morphology in trilayers

Figures 2–4 show subsurface views of contact-induced cracks in the glass/sapphire/polycarbonate trilayers, for $d_g = 1000 \mu\text{m}$ and $d_s = 500 \mu\text{m}$. Each sequence represents a different fracture mode, according to the specific surface abraded. The contact area is seen as the dark shadow with near-central light reflection spot. The first frame in each figure shows the contact near the critical load; subsequent frames show the ensuing crack evolution. We will confirm below (Fig. 5) that in each case cracking initiates at the preferentially abraded surfaces.

Figure 2 corresponds to specimens with the top surface of the glass layer abraded. A ring crack first initiates at this top surface immediately outside the contact [Fig 2(a)], propagates downward and outward [Fig. 2(b)], and finally develops into a full cone crack [Fig. 2(c)]. Fizeau fringes indicate the crack opening. This development into a full cone takes place over a load range of approximately 45 N , without any detectable load drop during initiation, indicating a somewhat stable crack.

Figure 3 corresponds to specimens with the bottom surface of the glass layer abraded. Radial cracks now initiate subsurface [Fig. 3(a)] on median planes through the load axis and extend radially outward as the load

increases [Figs. 3(b) and 3(c)]. The radial cracks multiply during the loading, with subsequent arms approximately bisecting adjacent predecessors. Initiation in this case is abrupt, occurring within successive frames in the video sequence, indicating a strong instability. Once popped in, however, the radials are highly stable and propagate with near-equal lengths.

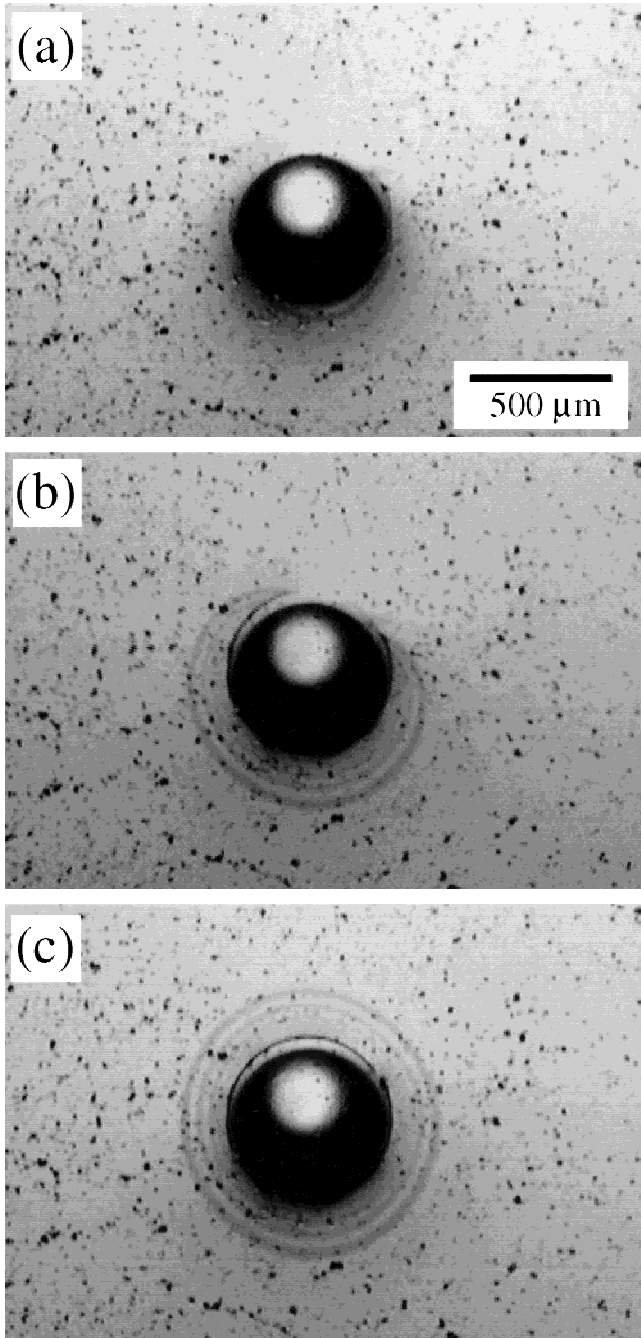


FIG. 2. *In situ* sequence showing crack evolution in trilayer of glass/sapphire coating, thicknesses $d_g = 1000 \mu\text{m}$ and $d_s = 500 \mu\text{m}$, on polycarbonate substrate. Contact tests were performed with a WC sphere, $r = 3.18 \text{ mm}$, (a) $P = 348 \text{ N}$, (b) $P = 370 \text{ N}$, and (c) $P = 393 \text{ N}$. A cone crack initiates at the top-abraded glass surface.

Figure 4 corresponds to specimens with the bottom surface of the sapphire layer abraded. Subsurface radial cracks now initiate in the sapphire. In this case the initiation is even more abrupt than in the glass—

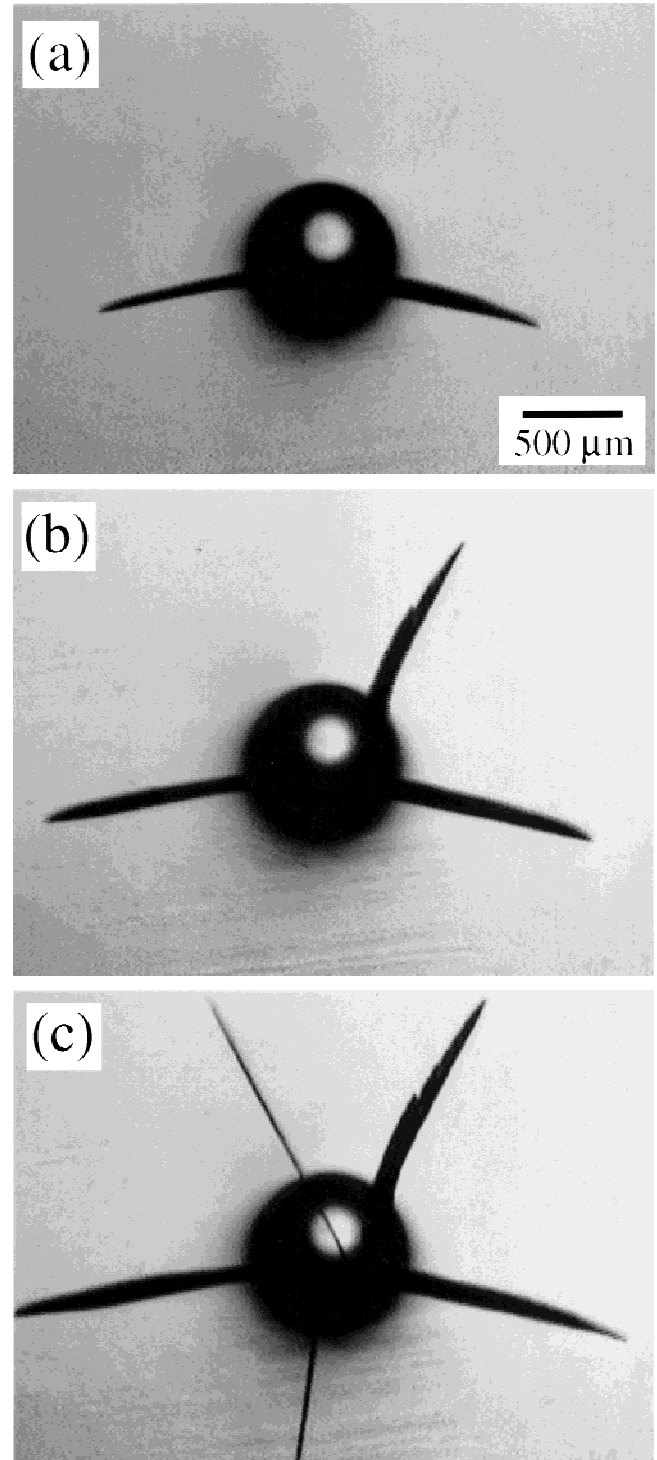


FIG. 3. *In situ* sequence showing crack evolution in trilayer of glass/sapphire coating, thicknesses $d_g = 1000 \mu\text{m}$ and $d_s = 500 \mu\text{m}$, on polycarbonate substrate. Contact tests were performed with a WC sphere, $r = 3.18 \text{ mm}$, (a) $P = 675 \text{ N}$, (b) $P = 724 \text{ N}$, and (c) $P = 766 \text{ N}$. Radial cracks initiate at the bottom-abraded glass surface.

Figs. 4(a) and 4(b) again represent successive video frames—with an audible ping at pop in and a noticeable load drop (>20 N relative to peak load 435 N). The crack arms in Fig. 4(b) extend well outside the field of view, to approximately 3 mm radial dimension. Note the appearance of only two diametrically opposed arms in Fig. 4(b), suggesting an even more unstable pop in than in the glass.

Side views of the different crack systems are shown in Fig. 5. Figure 5(a) represents a specimen with top-abraded glass layer at relatively high load [cf. Fig. 2(c)]. A cone crack forms at the abraded contact surface and spreads sideways at an angle approximately 22° to this surface.^{26–28} Note that this crack penetrates only a small

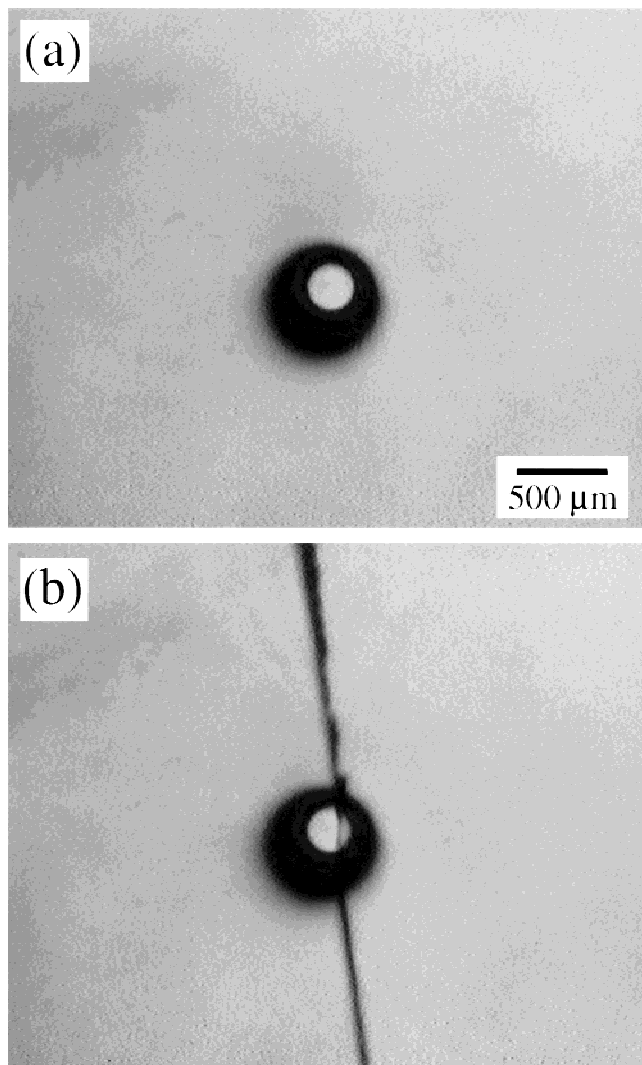


FIG. 4. *In situ* sequence showing crack evolution in trilayer of glass/sapphire coating, thicknesses $d_g = 1000 \mu\text{m}$ and $d_s = 500 \mu\text{m}$, on polycarbonate substrate. Contact tests were performed with a WC sphere, $r = 3.18$ mm, and $P = 435$ N with load drop approximately 20 N between consecutive video frames. The radial crack initiates at the bottom-abraded sapphire surface.

depth relative to the glass thickness. Figure 5(b) represents a specimen with bottom-abraded glass layer, again at high load [compare Fig. 3(c)]. The crack initiates at the bottom-abraded surface of the glass and grows radially along a median plane parallel to the field of view, over a radial distance of approximately 2 mm. Figure 5(c) shows a specimen with bottom-abraded sapphire layer, at load just above critical for sapphire [compare Fig. 4(b)] but considerably lower than for glass [Fig. 5(b)], with radial crack dimension approximately 3 mm. The radial cracks in Figs. 5(b) and 5(c) remain completely confined to the layer within which they initiate.

For comparison, Fig. 6 shows crack initiation in a specimen with no layer surfaces abraded at all. Radial fracture initiates in the sapphire, at much higher critical load than in any of the abraded specimens (compare Figs. 2–4). The initiation is extremely abrupt [Figs. 6(a)–6(c) once more represent successive frames], with copious crack multiplications, markedly loud acoustic emissions, and rapidly successive load drops (>175 N relative to peak value 950 N).

Despite the abrupt nature and exaggerated scale of cracking in some of the above cases, especially the radial cracking in Fig. 6, the specimens all remain intact, suggesting that the trilayer structures are highly damage-tolerant.

B. Critical loads

Critical loads P_{rad} and P_{cone} for layer fracture in the glass/sapphire/polycarbonate trilayers are plotted in Figs. 7 and 8, as a function of sapphire thickness d_s for fixed glass thickness $d_g = 1$ mm. Each data point in these figures represents the mean and standard deviation of 5 to 10 indentations.

Figure 7 shows P_{rad} and P_{cone} data for cracking in the glass layers, for bottom-abraded and top-abraded surfaces respectively. The P_{rad} data decline markedly with diminishing d_s . For now, we represent the trend in these data by the FEM-generated solid curve for a nominal glass/sapphire adhesive thickness $h = 10 \mu\text{m}$ (Sec. IV). (As we shall show later, the P_{rad} data for glass are quite sensitive to h , accounting for apparent deviations between data and prediction.) The P_{cone} data actually increase with diminishing d_s . For reference, P_{cone} for monolithic abraded glass is included as the horizontal dashed line—as may be expected, the P_{cone} data are comparable with the monolithic value at higher d_s .

Figure 8 shows $P_{\text{rad}}(d_s)$ data for sapphire, for specimens with bottom surface abraded and unabraded. The data trends are similar for the two conditions but with higher P_{rad} for the unabraded surfaces, consistent with a lower flaw size in the latter case. The solid curves are from FEM analysis (Sec. IV). Comparing the values of critical loads for abraded sapphire layers in Fig. 8 with

those for abraded glass layers in Fig. 7, we note that $P_{\text{rad}}(\text{s}) < P_{\text{rad}}(\text{g})$ for all d_s values and that $P_{\text{cone}}(\text{g}) < P_{\text{rad}}(\text{s})$ except (by extrapolation) at $d_s \leq 350 \mu\text{m}$.

No delamination of the adhesively joined interfaces was observed in any of our experiments, over the range of experimental conditions covered.

C. Materials characterization

Results from subsidiary materials characterization tests are shown in Figs. 9 and 10. Figure 9 plots indentation stress–strain data for bulk glass, sapphire, polycarbonate, epoxy adhesive, and tungsten carbide materials. The stress–strain data for the glass and sapphire are linear, indicating an elastic response, over the stress range covered (up to the point of fracture). The data for the other materials, especially the polycarbonate and epoxy, indicate some plasticity at low stresses. These data provide essential material parameters for following stress analysis. Solid curves in Fig. 9 are FEM best-fit data evaluations (Sec. IV).

Figure 10 is a plot of critical load P_{rad} versus coating thickness d for glass/polycarbonate and sapphire/polycarbonate bilayers. Data obtained in the present experiments are shown as filled symbols—data from a previous study on glass/polycarbonate bilayers¹⁷ are included as unfilled symbols. Error bars are standard deviations, 5 to 10 indentations. Solid curves are FEM best fits (Sec. IV).

IV. STRESS ANALYSIS

Finite element modeling is used to analyze the stresses in the trilayer glass/sapphire/polycarbonate structures and to relate these stresses to the measured critical loads for radial cracking. The procedure is analogous to that described previously¹¹ but here using ABAQUS/Standard software (Hibbitt, Karlsson & Sorensen, Inc., Pawtucket, RI). The algorithm models a deformable tungsten carbide half-sphere indenter, radius $r = 3.18 \text{ mm}$, in frictionless axisymmetric contact with a flat deformable trilayer system 8-mm radius and 14-mm total thickness, bonded by infinitely strong interlayers. The simulation is performed by first setting the sphere in contact with the flat specimen and then loading to peak value in 70 equal increments.

The FEM grid for the layer system is shown in Fig. 11. The trilayer grid consists of 58,755 axisymmetric quadrilateral elements, each with 4 nodes. The minimum dimensions of the elements in the vicinity of the interfaces of primary interest are $4 \times 8 \mu\text{m}$ in the glass, sapphire, and polycarbonate layers and $2 \times 8 \mu\text{m}$ in the thinnest adhesive layers. The sphere grid consists of approximately 5263 elements.

For each layer, a uniaxial constitutive elastic–plastic stress–strain function $\sigma(\epsilon)$ is prescribed. Initially, each material deforms elastically, as defined by Young's modulus E and Poisson's ratio ν . Above some yield

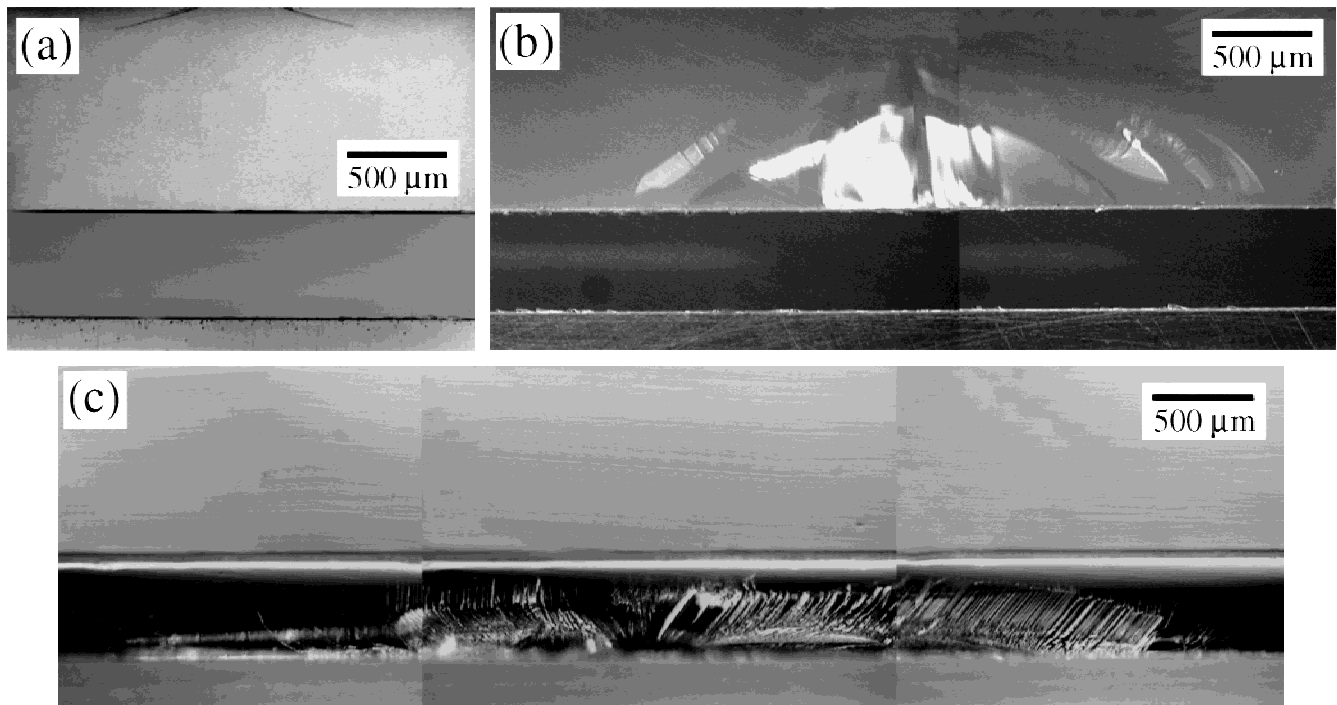


FIG. 5. Optical micrographs showing crack profiles in sectioned trilayer of glass/sapphire coating, thicknesses $d_g = 1000 \mu\text{m}$ and $d_s = 500 \mu\text{m}$, on polycarbonate substrate, after contact with a WC sphere, $r = 3.18 \text{ mm}$: (a) cone crack in top-abraded glass surface, $P = 700 \text{ N}$ (compare Fig. 2); (b) radial crack in bottom-abraded glass, $P = 800 \text{ N}$ (compare Fig. 3); (c) radial crack in bottom-abraded sapphire, $P = 430 \text{ N}$ (compare Fig. 4). [Figures 5(b) and 5(c) are composite mosaics.]

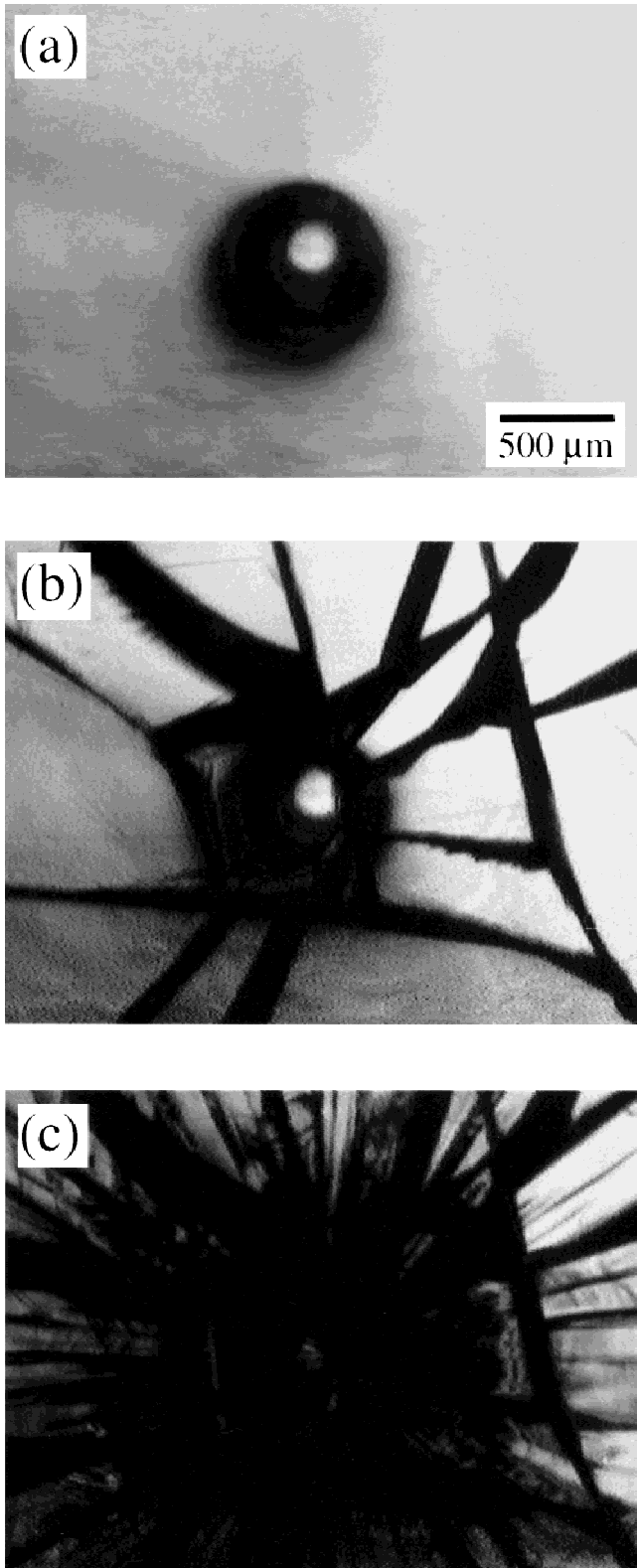


FIG. 6. *In situ* sequence showing crack evolution in trilayer of glass/sapphire coating, thicknesses $d_g = 1000 \mu\text{m}$ and $d_s = 500 \mu\text{m}$, on polycarbonate substrate. Contact tests were performed with a WC sphere, $r = 3.18 \text{ mm}$, and $P = 949 \text{ N}$ with load drops totalling $>175 \text{ N}$ in consecutive video frames. The radial cracks initiate at the unabraded sapphire surface.

stress Y the materials deform according to a critical shear stress condition with linear strain hardening.²⁹ The uniaxial stress–strain relation has the form

$$\sigma = E\epsilon \quad (\sigma \leq Y) \quad , \quad (1a)$$

$$\sigma = Y + \alpha(\epsilon E - Y) \quad (\sigma \geq Y) \quad , \quad (1b)$$

where α is a dimensionless strain-hardening coefficient with value between 0 (fully plastic) and 1 (fully elastic). In this study, E and ν are measured independently by conventional sonic techniques and Y and α are iteratively adjusted by trial and error to fit the indentation stress–strain data for monolithic materials in Fig. 9 using the FEM algorithm. Results of these evaluations are included in Table I.

With these parameter evaluations, the FEM simulation is then used to compute principal stresses $\sigma_1 \geq \sigma_2 \geq \sigma_3$ in the trilayer structures. The cone cracks are governed by the σ_1 stress field in the near-contact region at the top surface. Such near-contact fields have been well documented³⁰ and are only slightly affected by the presence of the underlying layers.^{11,31} Of primary interest here are the radial cracks, governed by the far-field σ_2 (hoop) stresses.¹⁷ Contours of σ_2 are shown in Fig. 12 for a glass/sapphire/polycarbonate trilayer (layer thicknesses $d_g = 1000 \mu\text{m}$ and $d_s = 500 \mu\text{m}$), (a) *with* adhesive ($h = 10 \mu\text{m}$) and (b) *without* adhesive ($h = 0$) at a *fully bonded* glass/sapphire interface, at load $P = 435 \text{ N}$ (corresponding to fracture in the sapphire layer—compare Fig. 4), in regions of tension (compression regions indi-

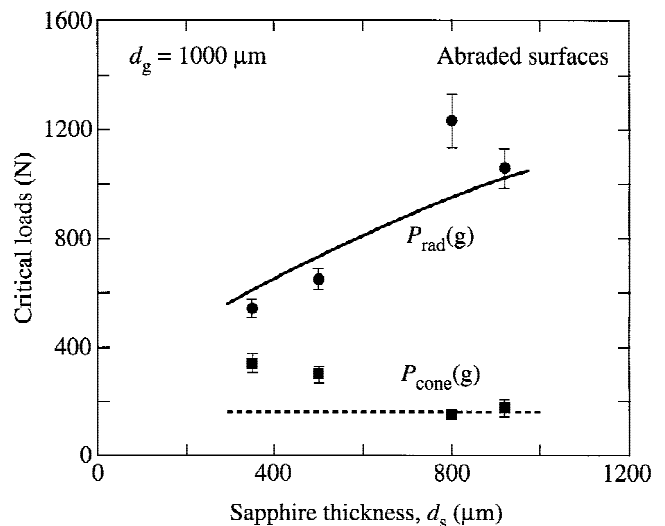


FIG. 7. Critical loads P_{cone} and P_{rad} for fracture in glass layers as function of sapphire thickness d_s in glass/sapphire/polycarbonate trilayers, for fixed glass thickness $d_g = 1000 \mu\text{m}$. Contact tests were performed with WC sphere, $r = 3.18 \text{ mm}$, with top glass surfaces (cone cracks) or bottom glass surfaces (radial cracks) abraded. Each data point represents mean and standard deviation from 5 to 10 tests. The solid curve is an FEM prediction of $P_{\text{rad}}(d_s)$ for nominal adhesive thickness $h = 10 \mu\text{m}$. The horizontal dashed line is the experimental P_{cone} value for top-abraded monolithic glass.

cated by black background). Maxima in these stresses in both the glass and sapphire layers occur at the bottom surfaces along the contact axis. The tensile stress intensity is markedly greater in the sapphire than in the glass, indicating substantial stress transfer to the stiffer member of the composite glass/sapphire coating bilayer. The pronounced lateral spread in the contours along the bottom surface of the sapphire layer and confinement of the tensile stresses to the bottom portion of the layer are consistent with the crack geometry seen in Fig. 5(c). Note that removing the glass/sapphire adhesive interlayer in Fig. 12(b) (but retaining full interfacial bonding) totally eliminates any tensile stress in the glass layer but does not strongly disturb the stress contours at the sapphire bottom surface.

To evaluate critical loads for radial cracking in the trilayers using the FEM algorithm, it is necessary first to determine strengths σ_F for glass and sapphire. We do this here by adjusting σ_F values to give the best-fit solid curves to the subsidiary bilayer data for bottom-abraded glass and sapphire coatings on polycarbonate substrates in Fig. 10. Strength values obtained in this way are included in Table I. Next we generate σ_2 maxima in the glass and sapphire in the trilayer structures as a function of increasing P . Figure 13 shows $\sigma_2(P)$ plots for the actual d_s values investigated in the experiments of Figs. 7 and 8 but for a nominal fixed adhesive thickness $h = 10 \mu\text{m}$. There is a marked change in slope in the curves for the glass layer at $P \approx 350 \text{ N}$ in Fig. 13(a). The FEM results show that at this point the maximum

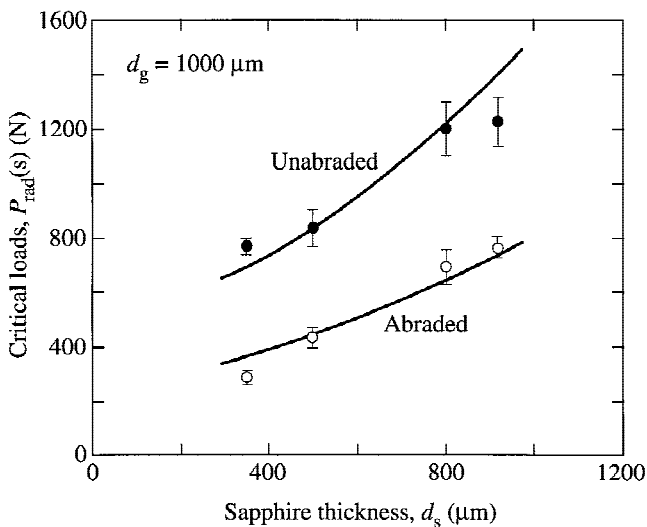


FIG. 8. Critical loads P_{rad} for fracture in sapphire layers as function of d_s for glass/sapphire/polycarbonate trilayers, fixed glass thickness $d_g = 1000 \mu\text{m}$. Contact tests were performed with a WC sphere, $r = 3.18 \text{ mm}$, with bottom sapphire surfaces abraded or all surfaces unabraded. Each data point represents mean and standard deviation from 5 to 10 tests. Solid curves are FEM predictions of $P_{\text{rad}}(d_s)$ for bottom-abraded and unabraded sapphire surfaces, nominal adhesive thickness $h = 10 \mu\text{m}$.

shear stress in the epoxy adhesive at the glass/sapphire interlayer exceeds the limit $Y/2$ for yield, facilitating greater flexure and hence tensile stress buildup in the glass overlayer. On the other hand, the influence of glass/sapphire adhesive yield is barely detectable in the plots for the sapphire intermediate layer in Fig. 13(b), especially at the bottom surfaces. Our computations reveal no yield elsewhere in the trilayer structures (including in the adhesive at the sapphire/polycarbonate interface) over the load ranges of our experiments. Intersection points of the strengths σ_F (horizontal dashed lines) with the $\sigma_2(P)$ curves in Fig. 13 determine FEM-evaluated critical loads for radial cracking (vertical dashed lines). $P_{\text{rad}}(d_s)$ functions representing these FEM determinations are included as the solid curves in Figs. 7 and 8. Note that these curves intersect the experimental data for the sapphire layer in Fig. 8 but not for the glass layer in Fig. 7. As shown in Table II, refined calculations using *actual*

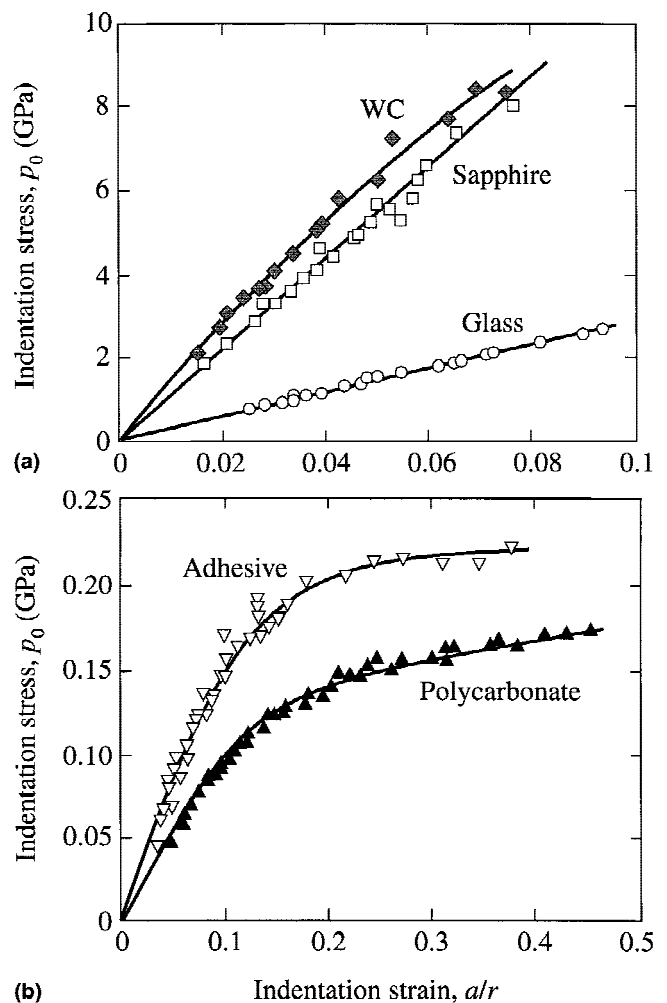


FIG. 9. Indentation stress–strain data for monolithic materials used in the contact tests: (a) glass, sapphire, and tungsten carbide; (b) polycarbonate and epoxy adhesive. (Note different scales in the two plots.) Contact tests performed with WC spheres, $r = 1.98$ to 12.7 mm . Solid curves through experimental data are FEM-generated functions.

rather than *nominal* adhesive thicknesses in the FEM algorithm provide improved agreement between prediction and experiment. (Again, the same refinements produce undetectable shifts in the predicted values for the sapphire layer.) This comparison affirms a critical role of the glass/sapphire adhesive layer in the radial fracture of the glass but not of the sapphire. On the other hand, the sapphire/polycarbonate adhesive has relatively minor influence on the fracture properties—recall that the properties of the adhesive are very similar to those of the polycarbonate (Table I), so that this second adhesive interlayer may be regarded as part of the substrate.¹⁷

Included in Fig. 8 is an FEM fit to the sapphire data for trilayers with all surfaces unabraded, using $\sigma_F = 800$ MPa (compare 544 MPa for abraded sapphire surfaces, Table I), reflecting smaller flaw sizes in the as-received state.

V. DISCUSSION

We have studied contact-induced transverse fracture modes in trilayers consisting of brittle bilayer coatings on soft substrates. Specifically, we have investigated transparent glass/sapphire/polycarbonate trilayers, using a simple epoxy adhesive to bond adjacent layers. The transparency of this model system uniquely enables *in situ* observations of different cracking modes during actual contact testing, including subsurface radial cracks in the glass *and* the sapphire layers as well as conventional cone cracks at the top glass surface, Figs. 2–4. Preabrasion of selected layer surfaces facilitates observation of each crack mode separately and reproducibly.

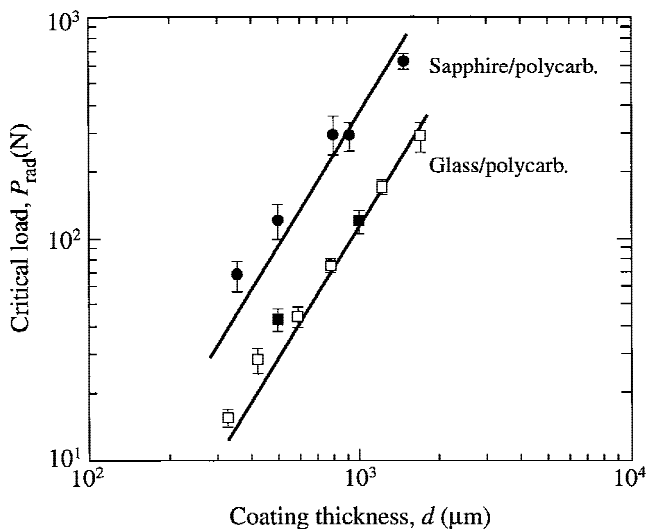


FIG. 10. Critical loads P_{rad} for fracture versus coating thickness d (d_g or d_s) in glass/polycarbonate and sapphire/polycarbonate bilayers. Contact tests performed with a WC sphere, $r = 3.18$ mm, and bottom coating surfaces abraded. Each data point represents mean and standard deviation from 5 to 10 tests. Unfilled symbols are data from Ref. 17. Solid lines are FEM best fits.

Side views in specimens sectioned *a posteriori* through the indentations confirm the fracture origins and provide important supplementary information on the various crack geometries in the glass and sapphire layers, Fig. 5. Whereas cone cracks are shallow and do not penetrate deeply into the glass, radial cracks spread over comparatively long lateral distances, most dramatically in the sapphire layers. However, even the longest radial cracks remain confined to the bottom surface region of each abraded layer. In unabraded specimens, radial cracks initiate in the sapphire layers at higher loads and develop into more complex fracture networks, Fig. 6 (compare Fig. 4). But again, the specimens remain intact, indicating a degree of damage tolerance. Our observations suggest that, in opaque coatings, even large radial cracks (especially those that form in intermediate layers) may generally pass unnoticed in routine surface inspections.

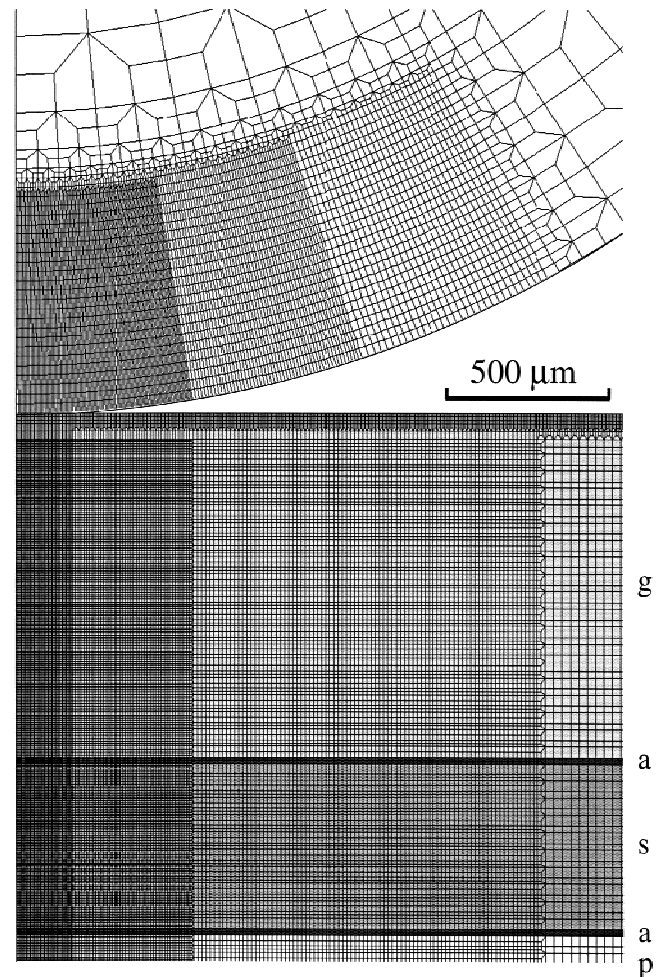


FIG. 11. FEM grid used to simulate Hertzian contact in glass/sapphire/polycarbonate (g/s/p) trilayers, with interlayer joined by adhesive (a), showing a half-section through axisymmetric configuration. The grid is shown for WC sphere radius $r = 3.18$ mm, coating thicknesses $d_g = 1000$ μm and $d_s = 500$ μm , and adhesive thickness $h = 10$ μm .

Critical load data have been obtained for the trilayers for each transverse fracture mode. Cone crack loads are relatively insensitive to sapphire thickness d_s , Fig. 7. Radial crack loads are more sensitive to d_s , with $P_{\text{rad}}(\text{g}) > P_{\text{rad}}(\text{s})$, Figs. 7 and 8. Generally, $P_{\text{rad}} > P_{\text{cone}}$, except for $P_{\text{rad}}(\text{s})$ at $d_s \leq 350 \mu\text{m}$ in the bottom-abraded sapphire. In the event that the glass top surfaces are unabraded, first fracture occurs as radial cracking at the bottom surface of one of the coating layers—if both bottom surfaces are prepared in the same way (abraded *or* unabraded), the radial cracks form first in the sapphire. Thus the sapphire layer, despite its markedly superior stiffness and strength properties relative to glass, is susceptible to premature fracture in our system, especially at small d_s . This suggests that one should pay proper attention to optimizing the strength of the supporting stiff intermediate layer.

FEM is helpful in understanding several aspects of the crack morphologies and critical load data. Cone cracks are governed by σ_1 principal stresses, and radial

cracks by σ_2 hoop stresses.¹⁷ We have focused our attention on the radial cracks, assuming initiation when σ_2 exceeds the strength σ_F of bulk glass or sapphire (an assumption that breaks down for cone cracks, where the σ_1 stresses are highly inhomogeneous over depths of the initial starting flaws.^{27,32}) The σ_2 stress contours in Fig. 12(a) are consistent with the observed elongate profiles of the radial cracks in the glass and (especially) the sapphire [Figs. 5(b) and 5(c)]. The FEM computations also provide quantitative confirmation of the critical load data, notably the dependence on sapphire layer thicknesses in Figs. 7 and 8 [notwithstanding the systematic deviations apparent in the bilayer $P_{\text{rad}}(d)$ plots in Fig. 10].

The FEM calculations are especially valuable in demonstrating the crucial role of any intervening soft adhesive interlayer at the glass/sapphire interface in the

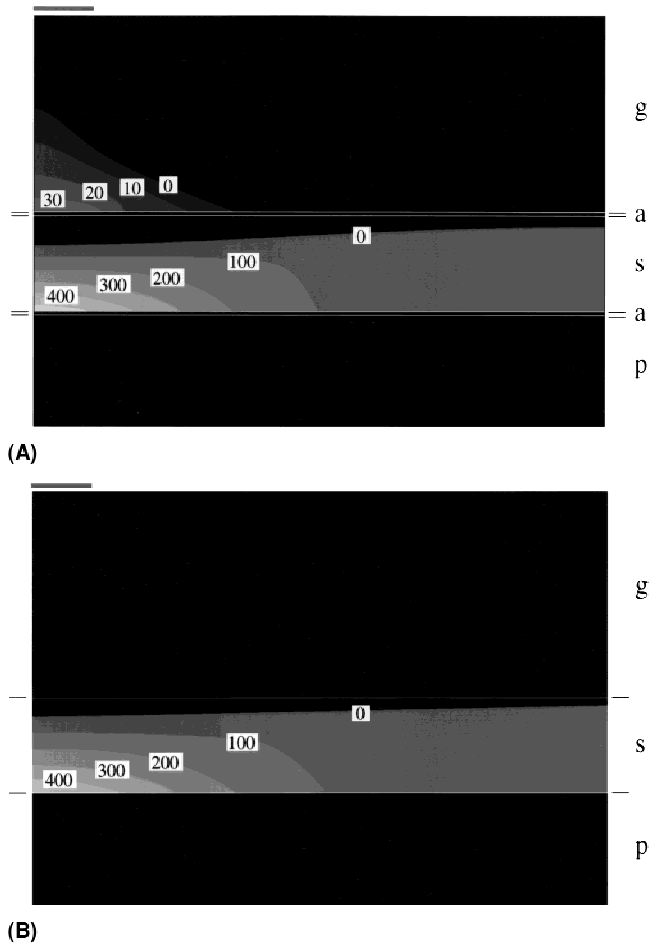


FIG. 12. FEM-generated σ_2 stress contours (MPa) in glass/sapphire/polycarbonate (g/s/p) trilayers, $d_g = 1000 \mu\text{m}$ and $d_s = 500 \mu\text{m}$, from contact with WC sphere, $r = 3.18 \text{ mm}$ at $P = 435 \text{ N}$ (cf. Fig. 4): (A) with glass/sapphire adhesive (a), $h = 10 \mu\text{m}$; (B) without glass/sapphire adhesive, $h = 0$. The contact radius is indicated at the top surface.

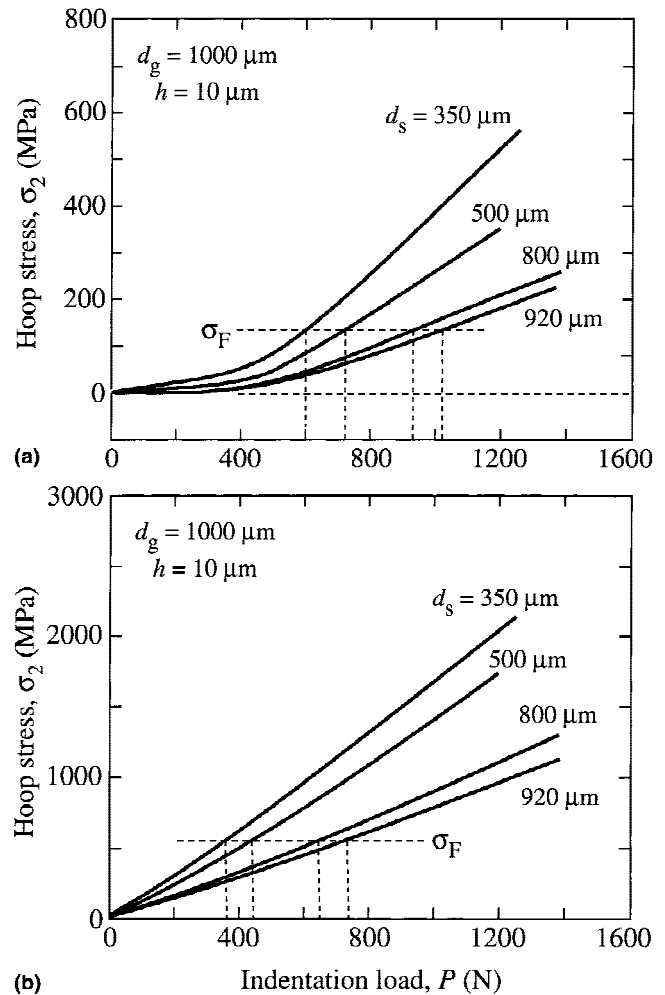


FIG. 13. FEM-generated plots of maximum hoop tensile stresses σ_2 in bottom surfaces of (a) glass and (b) sapphire layers in glass/sapphire/polycarbonate trilayer structures as function of contact load P . Computations for a WC sphere, $r = 3.18 \text{ mm}$, fixed thicknesses $d_g = 1000 \mu\text{m}$ and $h = 10 \mu\text{m}$, for specified d_s values. Dashed horizontal lines are strengths (from Fig. 10). Radial cracks are assumed to initiate at load $P = P_{\text{rad}}$ (vertical dashed lines) when σ_2 equals the bulk strength σ_F of the abraded glass or sapphire (horizontal dashed line).

generation of radial fractures in the glass, by enabling flexure in the upper glass layer. Our FEM calculations reveal the epoxy in this interlayer to undergo yield at an early stage in the loading [approximately 350 N, Fig. 13(a)], further enhancing this flexure. Removing this interlayer in the FEM mesh eliminates all tensile stresses in the glass layer (Fig. 12), *averting the risk of radial fracture in the glass*. Accurate accounting of actual adhesive thicknesses h in the FEM mesh is therefore essential for obtaining quantitative agreement with experimental P_{rad} values for glass (Table II). At the same time, since the elastic–plastic properties of the epoxy are similar to those of the polycarbonate (Table I), removal of the underlying adhesive at the sapphire/polycarbonate interlayer has virtually no effect on any fracture mode.

No delamination was observed in our experiments, despite the above-mentioned yield in the glass/sapphire adhesive. However, more adverse mechanical conditions, e.g., exceptionally high or cyclic loads, could well induce incipient delaminations. This would appear to be another good reason to remove soft interlayers between outer and intermediate layers in real systems (e.g., as is done in porcelain-fused-to-alumina dental crowns). Our FEM calculations indicate that, with such interlayer removed, all components in the entire trilayer system remain well within the elastic region over the load range covered, affording adequate protection to a soft substrate.

The attention to model transparent systems in the present study does not detract from the generality of our approach. With the validity of the FEM algorithm established, we may use the FEM code to explore beyond the range of variables covered in our experiments and even to extend to other systems or more complex geometries (e.g., dental crowns, cutting tools). We illustrate in Fig. 14 by plotting critical loads for first fracture in our trilayer system with either glass or sapphire as top layer, as a function of composite coating thickness $d = d_s + d_g$ over a range of $d = 10^2$ to 10^4 μm , for hypothetical specimens without adhesive and with surfaces abraded. We consider specifically glass/sapphire/polycarbonate and sapphire/glass/polycarbonate trilayers with equal glass and sapphire thicknesses, along with glass/

polycarbonate and sapphire/polycarbonate bilayers as limiting cases. Accordingly, in Fig. 14 the inclined lines are plots of FEM-generated $P_{\text{rad}}(d)$ functions for first radial cracking, in either the glass (dashed lines) or sapphire (solid lines). In sapphire/glass/polycarbonate, tension exists in the lower surface of the sapphire as well as in the glass—indeed, in this case the estimated P_{rad} is about the same in the sapphire and the glass. The critical loads for radial cracking are higher for sapphire underlayers relative to glass underlayers at any given thickness. The horizontal lines are corresponding experimental critical loads for Hertzian cracking in abraded glass and sapphire monoliths (here neglecting any effects of the underlayer on P_{cone}). From a design standpoint, it is desirable to operate the coating structure in the region below the bounding $P_{\text{rad}}(d)$ or P_{cone} lines. Note the relatively small shifts between the different $P_{\text{rad}}(d)$ lines, suggesting that composite coating thickness is a more important variable than constituent material properties (elastic moduli). Notwithstanding these small shifts, it would appear preferable to use the stiffer material (sapphire) as the intermediate, support layer, first to lessen the chance of initiating the more dangerous radial cracks and second to contain any such cracks within the sub-surface layers once they initiate.

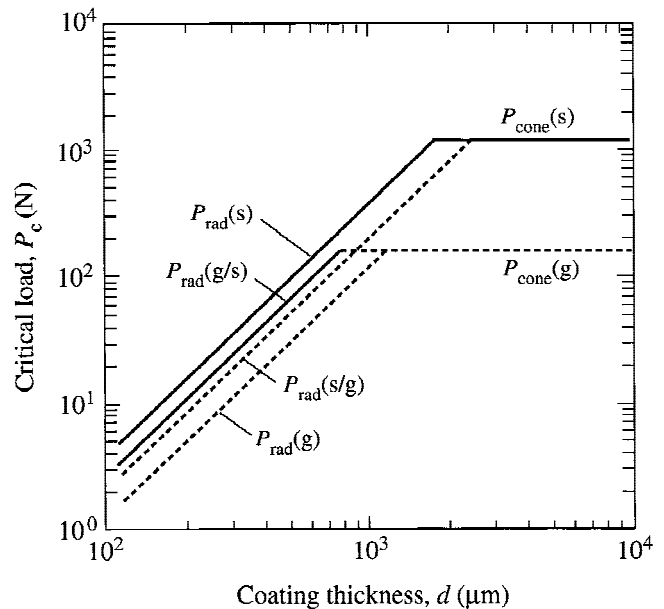


Fig. 14. Critical fracture loads for layer structures without adhesive and with surfaces abraded, as a function of composite bilayer thickness $d = d_s + d_g$. Results are for glass/polycarbonate bilayers ($d_g = d$, $d_s = 0$), sapphire/polycarbonate bilayers ($d_s = d$, $d_g = 0$), glass/sapphire/polycarbonate trilayers ($d_g = d/2 = d_s$), and sapphire/glass/polycarbonate trilayers ($d_s = d/2 = d_g$). Inclined lines are FEM predictions of $P_{\text{rad}}(d)$ for specified values of d_s/d , and horizontal lines are experimental values of P_{cone} for abraded glass and sapphire monoliths. Solid lines indicate fracture in sapphire, and dashed lines fracture in glass.

TABLE II. Critical loads for radial cracks in bottom-abraded glass layers in trilayer structures, comparing experimental and FEM-calculated data for d_s values specified and $d_g = 1000$ μm and for actual measured values of h .

Sapphire thickness d_s (μm)	Adhesive thickness h (μm)	P_{rad} (expt) (N)	P_{rad} (FEM) (N)
350	12	544 ± 32	577 ± 17
500	15	654 ± 40	645 ± 20
800	7	1230 ± 100	1073 ± 33
920	9	1055 ± 70	1044 ± 36

Other factors remain to be considered in the analysis of failure of trilayers with brittle coatings. We have not considered potential rate effects in our experiments, e.g., slow crack growth in the brittle layers^{33,34} or viscoelastic deformation in the polymer substrate and adhesive layers.³⁵ Deformation properties of polymeric materials are also notoriously dependent on hydrostatic stress states,³⁶ here ignored in our assumption of a simple Tresca criterion for yield. Nor have we considered the mechanics of crack evolution beyond initiation and specifically how these cracks propagate (and perhaps interact) to ultimate failure. And there is the issue of flaw statistics in the failure of surfaces without controlled (abrasion) flaws (e.g., upper curve in Fig. 8). Finally, we have used a numerical algorithm FEM as our means of stress evaluation. A more analytical approach based on the theory of flexing plates on soft foundations is currently under investigation in our laboratories.

ACKNOWLEDGMENTS

Support for this work was provided by the Ministerio de Educación y Ciencia (DGICYT MAT 97-0562-C02-02) of Spain, by the U.S.–Spain Joint Committee for Scientific and Technological Cooperation (Grant 305), and by a National Institute of Dental Research grant (NIDR PO1 DE10976). Information on product names and suppliers in this paper is not to imply endorsement by NIST.

REFERENCES

- J.C. Knight, T.F. Page, and I.M. Hutchings, *Thin Solid Films* **177**, 117 (1989).
- R.A. Miller, *Surf. Coat. Technol.* **30**, 1 (1987).
- H. Herman, C.C. Berndt, and H. Wang, in *Ceramic Films and Coatings*, edited by J.B. Wachtman and R.A. Haber (Noyes Publications, Park Ridge, NJ, 1993), pp. 131–88.
- J.R. Kelly, *Annu. Rev. Mater. Sci.* **27**, 443 (1997).
- J.R. Kelly, *J. Prosthet. Dent.* **81**, 652 (1999).
- M.V. Swain and J. Mencik, *Thin Solid Films* **253**, 204 (1994).
- L. An, H.M. Chan, N.P. Padture, and B.R. Lawn, *J. Mater. Res.* **11**, 204 (1996).
- D.F. Diao, K. Kato, and K. Hokiigawa, *Trans. ASME J. Tribol.* **116**, 860 (1994).
- A. Pajares, L. Wei, B.R. Lawn, N.P. Padture, and C.C. Berndt, *Mater. Sci. Eng. A* **208**, 158 (1996).
- S. Wuttiaphan, B.R. Lawn, and N.P. Padture, *J. Am. Ceram. Soc.* **79**, 634–40 (1996).
- A.C. Fischer-Cripps, B.R. Lawn, A. Pajares, and L. Wei, *J. Am. Ceram. Soc.* **79**, 2619 (1996).
- H.M. Chan, *Annu. Rev. Mater. Sci.* **27**, 249 (1997).
- T.J. Lardner, J.E. Ritter, and G-Q. Zhu, *J. Am. Ceram. Soc.* **80**, 1851 (1997).
- K.S. Lee, S. Wuttiaphan, X.Z. Hu, S.K. Lee, and B.R. Lawn, *J. Am. Ceram. Soc.* **81**, 571 (1998).
- K.S. Lee, S.K. Lee, B.R. Lawn, and D.K. Kim, *J. Am. Ceram. Soc.* **81**, 2394 (1998).
- Y.G. Jung, S. Wuttiaphan, I.M. Peterson, and B.R. Lawn, *J. Dent. Res.* **78**, 887 (1999).
- H. Chai and B.R. Lawn, *J. Mater. Res.* **14**, 3805 (1999).
- H. Chai and B.R. Lawn, *J. Mater. Res.* **15**, 1017 (2000).
- J. Jitcharoen, N.P. Padture, A.E. Giannakopoulos, and S. Suresh, *J. Am. Ceram. Soc.* **81**, 2301 (1998).
- K.A. Malament and S.S. Socransky, *J. Prosthet. Dent.* **81**, 23 (1999).
- A.G. Mikosza and B.R. Lawn, *J. Appl. Phys.* **42**, 5540 (1971).
- M.V. Swain and B.R. Lawn, *Phys. Status Solidi* **35**, 909 (1969).
- M.V. Swain and J.T. Hagan, *J. Phys. D: Appl. Phys.* **9**, 2201 (1976).
- F. Guiberteau, N.P. Padture, H. Cai, and B.R. Lawn, *Philos. Mag. A* **68**, 1003 (1993).
- H. Cai, M.A. Stevens Kalceff, and B.R. Lawn, *J. Mater. Res.* **9**, 762 (1994).
- F.C. Roesler, *Proc. Phys. Soc. London B* **69**, 981 (1956).
- F.C. Frank and B.R. Lawn, *Proc. R. Soc. London A* **299**, 291 (1967).
- C. Kocer and R.E. Collins, *J. Am. Ceram. Soc.* **81**, 1736 (1998).
- B.R. Lawn and D.B. Marshall, *J. Mech. Phys. Solids* **46**, 85 (1998).
- B.R. Lawn, *J. Am. Ceram. Soc.* **81**, 1977 (1998).
- H. Zhao, X.Z. Hu, M.B. Bush, and B.R. Lawn, *J. Mater. Res.* **15**, 676 (2000).
- S.K. Lee, S. Wuttiaphan, and B.R. Lawn, *J. Am. Ceram. Soc.* **80**, 2367 (1997).
- S.M. Wiederhorn, *J. Am. Ceram. Soc.* **50**, 407 (1967).
- S.M. Wiederhorn and L.H. Bolz, *J. Am. Ceram. Soc.* **53**, 543 (1970).
- S.J. Bennison, A. Jagota, and C.A. Smith, *J. Am. Ceram. Soc.* **82**, 1761 (1999).
- N.G. McCrum, C.B. Buckley, and C.P. Bucknall, *Principals of Polymer Engineering* (Oxford University Press, Oxford, United Kingdom, 1997).